

# Observational and Numerical Simulation Study of a Sequence of Eight Atmospheric Density Currents in Northern Spain

M. R. Soler · M. Udina · E. Ferreres

Received: 15 November 2013 / Accepted: 3 June 2014  
© Springer Science+Business Media Dordrecht 2014

**Abstract** A sequence of eight atmospheric density current fronts occurred in consecutive days are identified and analyzed using micrometeorological time series and numerical simulations. Observations were collected in the context of the INTERCLE project, which took place from September 2002 to November 2003 at the CIBA (Research Centre for the Lower Atmosphere) site located over the northern Spanish plateau. Numerical simulations used the Weather Research and Forecast (WRF) model with fine horizontal resolution (1 km). Both observations and simulations agree that the arrival of the density currents are characterized by a sharp change in temperature, wind velocity, wind direction and specific humidity and a source of intermittent turbulence. However, comparison between model and observations shows that the model predicts the intrusion of the density currents earlier than is observed. In addition, wavelet techniques applied to the data help distinguish the different scales present in the events, and therefore can reveal traces of gravity waves induced by the arrival of the density currents.

**Keywords** Density currents · Gravity waves · Intermittent turbulence · Nocturnal boundary layer · Numerical simulation · Wavelet transform

## 1 Introduction

As demonstrated by several studies and experimental campaigns (Cuxart et al. 2000; Poulos et al. 2002; Yagüe et al. 2007) the dynamics and properties of the nocturnal boundary layer (NBL), mainly over complex terrain, are difficult to predict due to typical global intermittency

---

M. R. Soler (✉) · M. Udina  
Department of Astronomy and Meteorology, Faculty of Physics,  
University of Barcelona, Martí i Franquès 1, 08028 Barcelona, Spain  
e-mail: rosa@am.ub.es

E. Ferreres  
Department of Applied Physics, Technical University of Catalonia,  
Av. Bases de Manresa, 61-73, 08240 Manresa, Spain

phenomena. Global intermittency or bursting, defined by Mahrt (1989) as the organization of turbulence in patches of eddies with large intervening areas of little turbulence activity, is a common characteristic of the NBL under clear-sky conditions (Nappo 1991; Mahrt 1999; Soler et al. 2002; Sun et al. 2002, 2004; Sun 2011; Terradellas et al. 2005). Despite the small fraction of the total time, such events occupy only the 20 % (Nappo 1991), the turbulence generated during these sporadic instability events becomes the primary mechanism for dispersion, and accounts for a major portion of the nighttime vertical transfer of heat, moisture and momentum (Coulter and Doran 2002). Several physical phenomena that may trigger intermittent turbulence and influence the structure and dynamics of the NBL have already been identified as wave instabilities (e.g., Blumen et al. 2001; Balsley et al. 2002; Fritts et al. 2003; Newsom and Banta 2003; Sun et al. 2004; Meillier et al. 2008; Viana et al. 2010; Udina et al. 2013), elevated jet maxima (e.g., Acevedo and Fitzjarrald 2003; Prabha et al. 2007; Cuxart and Jiménez 2007; Banta 2008) and density currents, sometimes called gravity currents or buoyancy currents (Sun et al. 2002; Adachi et al. 2004; Mayor 2011; Udina et al. 2013).

Here, we focus our study on gravity flows created by differences in the density of two adjacent fluids. They may occur in the atmosphere as a consequence, for example, of cold thunderstorm outflows or mesoscale circulations such as sea-breeze fronts and drainage flows, also known as katabatic winds, often originating and driven by topographical features in the absence of strong synoptic-scale forcing (Barry 1992; Mahrt et al. 2001; Soler et al. 2002; Maguire et al. 2006; Yagüe et al. 2007; Martínez and Cuxart 2009). Although several authors indicate that high-resolution mesoscale simulations are needed to better determine the origins and the structure of these mesoscale disturbances, little effort has been made in modelling them around the range of the meso- $\gamma$  scale. Thus, in this study, starting from an observational analysis in the context of the INTERCLE project (Estudio y parametrización de los intercambios de calor, humedad y momento en la Capa Límite Estable), we combine observations collected in the atmospheric boundary layer (ABL) with mesoscale meteorological modelling results. We use the Weather Research and Forecast (WRF) model with fine horizontal resolution (1 km), as some studies (Hu et al. 2010; Shin and Hong 2011; Arnold et al. 2012; Seaman et al. 2012) have stressed the importance of using high horizontal and vertical resolutions to capture ABL processes.

On the other hand, the arrival of density currents with sudden variations of different meteorological variables may result in vertical displacement of air parcels from their equilibrium position, which has been shown to be a common source of internal gravity waves (IGWs) (Chemel et al. 2009). These act as a modulator of the gravity current and may produce events of intermittent turbulence (Soler et al. 2002; Sun et al. 2002; Terradellas et al. 2005; Viana et al. 2009; Udina et al. 2013).

In recent years, to explore the aforementioned disturbances, Terradellas et al. (2005) and Viana et al. (2010), inter alia, showed that the wavelet method is a useful tool to identify and to analyse low frequency coherent structures such as gravity waves or density currents, and also higher frequency phenomena such as intermittent small scale turbulence. Knowledge of the dynamics of coherent structures and their interaction with turbulence is essential to improve our understanding of the mechanisms that govern the very stable boundary layer.

In the context of the INTERCLE project, we analyzed a large dataset containing measurements performed at different levels of the CIBA (Centro de Investigación de la Baja Atmósfera) tower (Conangla et al. 2008) with the aim of, (i) selecting intermittent turbulent episodes related to the intrusion of density currents; (ii) inferring which mesoscale circulations are associated with the density current irruptions using mesoscale meteorological

simulations, and (iii) exploring the formation of gravity waves induced by the density current using wavelet analysis.

The article is organized as follows: details of data collection, the studied area and a description of the wavelet method are presented in Sects. 2 and 3, respectively. The meteorological model, the Weather Research and Forecast (WRF), and the physical options used in this study are described in Sect. 4. Results provided by observations and simulations are presented in Sect. 5, including a brief description of the analyzed period and the arrivals of the density currents (5.1), the evaluation of the model against the tower and surface stations measurements (5.2), the vertical structure of the density current and the mesoscale fields overview (5.3). Finally, observed gravity waves are examined and discussed in Sect. 5.4 with particular emphasis on assessment of the information obtained using the wavelet method. A summary and our concluding remarks are given in Sect. 6.

## 2 Description of the Research Site and Data

The data used in this study were collected at the CIBA facilities. The CIBA is located in the central area of the Upper Duero basin, at  $41^{\circ}49'N$ ,  $4^{\circ}56'W$ . Several atmospheric boundary-layer experiments have been performed there, e.g. SABLES98 (Cuxart et al. 2000) and SABLES2006 (Yagüe et al. 2007), in order to study the properties and typical features of the stably-stratified nocturnal boundary layer, such as intermittent turbulence, slope flows, down-valley winds, low-level jets (LLJs) and gravity waves (Cuxart et al. 2000; Terradellas et al. 2001; Cuxart 2008; Bravo et al. 2008; Viana et al. 2007, 2009; Udina et al. 2013).

The Duero basin is surrounded by high mountain ranges at a distance of approximately 100 km to the north, east and south of the site (Fig. 1a), with the river flowing westwards towards the Atlantic (Fig. 1b). The CIBA sits on a small plateau known as Montes Torozos, which is a nearly flat area of  $800 \text{ km}^2$ , 840 m above sea level (a.s.l.) and approximately 50 m above the surrounding flat lands (Fig. 1b). Its central part is flat to the eye, but has gentle slopes ( $<1^{\circ}$ ) leading down to the Duero River. The plateau has a gentle downward slope of about 30 m along a stretch of 50 km from the north-east to the south-west, with the north-west and south-east borders slightly above the level of the inner plateau (Cuxart et al. 2000; Bravo et al. 2008).

The laboratory's main facility is a 100-m high mast equipped with fast-response sonic anemometers and a set of conventional sensors that measure wind speed and direction, air temperature and relative humidity at different heights (Table 1), as well as soil temperature and atmospheric pressure at the surface. A detailed description of the calculation of fluctuations can be found in Conangla et al. (2008).

## 3 Wavelet Methods

Here, we summarize the wavelet tools that are used to estimate kinetic energy and fluxes from time series of high-frequency meteorological data recorded under stable conditions. A description of the wavelet theory and application methods can be found in many reference works, e.g. Daubechies (1992), Torrence and Compo (1998) and Terradellas et al. (2005).

From the general principle that the wavelet transform fulfils energy conservation for the whole series (Mallat 1999), Terradellas et al. (2001) defined the energy density per time and scale unit of the time series  $f(t)$  at the scale parameter  $s$  and time  $t_0$  as,

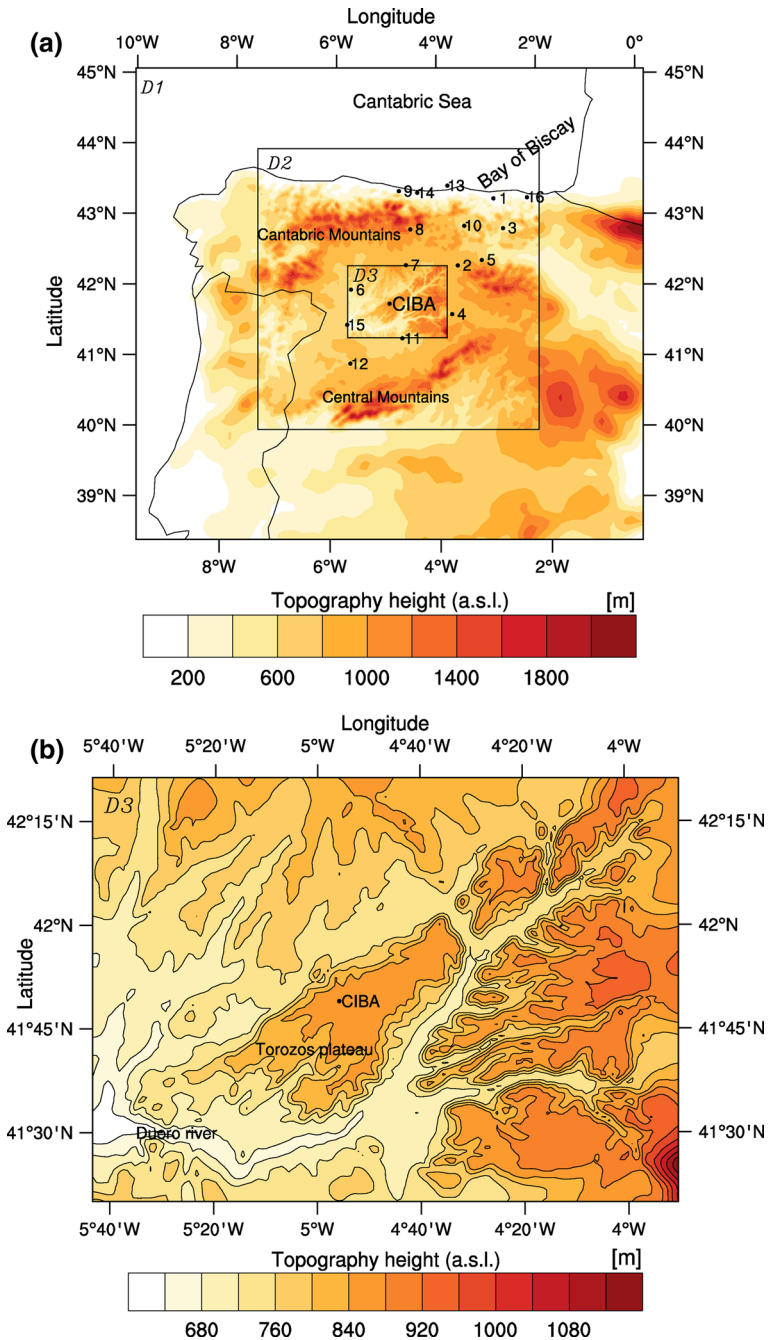


**Fig. 1** a Nested model domains D1, D2, D3 with 9-, 3- and 1-km resolutions, respectively; geographical location of the CIBA site; topography and emplacement of 15 surface meteorological stations within the domain D2 numbered from 1 to 15. b Detailed topography of the inner domain D3 with 40-m terrain height contours

**Table 1** Main instrumentation installed on the 100-m mast

Instrument	Heights (m)	Sampling rate (Hz)
Metek USA-1 sonic anemometers	5.6, 19.6, 49.6, 96.6	20
Wind vanes	9.6, 34.6, 74.6, 98.6	5
Cup anemometers	2.3, 9.6, 34.6, 74.6, 98.6	5
Platinum resistance thermometers	2.3, 10.5, 20.5, 35.5, 97.5	1
Humidity sensors	10, 97	5

$$\langle f^2 \rangle_{st_0} = \frac{2}{C_\Psi} \frac{\|F_{st_0}\|^2}{s^2}, \tag{1}$$

with

$$C_\Psi = 2\Pi \int_{-\infty}^{\infty} \frac{d\xi}{|\xi|} |\overline{\Psi(\xi)}|^2, \tag{2}$$

where  $F_{st_0}$  is the wavelet transform of the function  $f(t)$  at the scale parameter  $s$  and time  $t_0$  and  $\overline{\Psi(\xi)}$  is the Fourier transform of the mother wavelet. The integration over time and scale parameter in Eq. 1 for time series of wind components allows estimation of turbulent kinetic energy.

Similarly, Cuxart et al. (2002) defined what can be considered as the flux density,

$$\langle fg \rangle_{st_0} = \frac{2}{C_\Psi} \frac{F_{st_0} G_{st_0}^*}{s^2}, \tag{3}$$

where  $G_{st_0}$  is the wavelet transform of the function  $g(t)$  at the scale parameter  $s$  and time  $t_0$  and (\*) denotes complex conjugation. Integration of Eq. 3 allows estimation of the turbulent fluxes.

In the present study, the Morlet function—a plane wave with a Gaussian modulation—was chosen, because it is well suited to the analysis of series with oscillatory behaviour. Its expression is,

$$\Psi_{st_0}(t) = \frac{1}{\sqrt[4]{\Pi}} \frac{1}{\sqrt{|s|}} \exp \left[ i\omega_0 \left( \frac{t-t_0}{s} \right) \right] \exp \left[ -\frac{1}{2} \left( \frac{t-t_0}{s} \right)^2 \right], \tag{4}$$

where  $\omega_0$  is a non-dimensional parameter, usually called the base frequency. The scale parameter  $s$  is not the most appropriate magnitude to define the characteristics of an oscillation, because its value is meaningful only when associated with a particular mother wavelet. Meyers et al. (1993) derived the relationship between scale parameter and equivalent Fourier period for the Morlet wavelet,

$$T = \frac{1}{f} = \frac{4\Pi s}{\omega_0 + \sqrt{2 + \omega_0^2}}. \tag{5}$$

Introducing this expression to Eqs. 1 and 3, the specific contribution of a period to the total energy or flux is,

**Table 2** Model configuration options used for WRF simulations

	Domain 1	Domain 2	Domain 3
Horizontal grid	9 km	3 km	1 km
Dimensions ( $x, y, z$ )	88, 82, 48	145, 145, 48	154, 112, 48
Initial and boundary conditions	ECMWF $0.125^\circ \times 0.125^\circ$ every 6 h		
Simulated period	From 0000 UTC 3 July 2003 to 1200 UTC 11 July 2003		
Radiation	Dudhia scheme for shortwave radiation. RRTM for longwave radiation		
Land surface	NOAH land-surface model (4 subsoil layers)		
Microphysics	New Thompson et al. scheme		
PBL	Mellor–Yamada–Janjic scheme (MYJ)		
Surface layer	Eta surface-layer scheme		

$$\langle f^2 \rangle_{T_{t_0}} = \langle f^2 \rangle_{s_{t_0}} \left| \frac{ds}{dT} \right| = \frac{1}{C_\Psi} \frac{8\Pi}{\omega_0 + \sqrt{2 + \omega_0^2}} \frac{\|F_{s_{t_0}}\|^2}{T^2}, \quad (6)$$

$$\langle fg \rangle_{T_{t_0}} = \langle fg \rangle_{s_{t_0}} \left| \frac{ds}{dT} \right| = \frac{1}{C_\Psi} \frac{8\Pi}{\omega_0 + \sqrt{2 + \omega_0^2}} \frac{F_{s_{t_0}} G_{s_{t_0}}^*}{T^2}. \quad (7)$$

#### 4 Numerical Model

Simulations were made with the WRF modelling system, a state-of-the-art mesoscale numerical weather prediction system. We used version 3.3.1 with the Advanced Research WRF (ARW) dynamics solver designed for both research and operational applications (Skamarock et al. 2008). It is a fully-compressible non-hydrostatic model, with a terrain-following vertical coordinate; the horizontal and vertical grid staggering is of Arakawa C-grid type. The model configuration (Table 2) consists of three domains centred on the location of the CIBA meteorological tower, with horizontal resolutions of 9, 3 and 1 km (Fig. 1a). Domains 1 (9 km), 2 (3 km) and 3 (1 km) are run in two-way nesting from 0000 UTC 3 July to 1200 UTC 11 July 2003 and the first 12 h are treated as spin-up. Fields are saved every 5 min.

The analysis focuses on domains 2 and 3 (Fig. 1) since their high resolution (3 and 1 km, respectively) allows the details of the flow over the Duero basin and Montes Torozos plateau to be captured. In the vertical, 48 sigma levels are used from the ground up to 100 hPa for all the domains with the first level 2 m above the surface, and the first 13 levels all within the first 100 m. Initial and boundary conditions are taken from the ERA-Interim analysis from the European Centre for Medium Range Weather Forecasts (ECMWF) which has a horizontal resolution of  $0.125^\circ$  and the boundary conditions are forced every 6 h.

The physics package includes the rapid radiative transfer model (RRTM) scheme for longwave radiation (Mlawer et al. 1997), the Dudhia scheme for shortwave radiation (Dudhia 1989), the New Thompson microphysics scheme (Thompson et al. 2004), the Noah land-surface scheme (Chen and Dudhia 2001) and no cumulus parametrization is used as the resolution is fine enough to resolve convective eddies. For the planetary boundary-layer (PBL) parametrization we select the Mellor–Yamada–Janjic (MYJ) scheme (Janjić 1990, 1996, 2002) and for the surface layer, the Eta scheme. Here, special emphasis is devoted to PBL parametrizations as they play an important role in PBL meteorological fields simulated

by the model. The MYJ scheme uses the 1.5-order (level 2.5) local turbulence closure model of Mellor and Yamada (1982) to represent turbulence above the surface layer, and determines eddy-diffusion coefficients from the turbulent kinetic energy (TKE) forecasted by the model. Several studies have compared different PBL parametrizations in the WRF model (Hu et al. 2010), showing that local TKE closure schemes perform better than first-order approaches (Shin and Hong 2011; Udina et al. 2013).

Currently, each PBL parameterization is tied to a particular surface-layer scheme in the WRF model, therefore the Eta surface-layer scheme (Janjić 1996, 2002) based on similarity theory (Monin and Obukhov 1954) is coupled to the MYJ model. The scheme includes parametrization of the viscous sub-layer; over water surfaces, the viscous sub-layer is parametrized explicitly following Janjić (1994). Over land, the effects of the viscous sub-layer are taken into account through a variable roughness length for temperature and humidity as proposed by Zilitinkevich (1995). The Beljaars (1994) correction is applied in order to avoid singularities in the case of free convection and vanishing wind speed (and consequently  $u_*$ ). The surface fluxes are computed by an iterative method.

## 5 Results

### 5.1 Overview of the Period and Arrival of the Density Current

After exhaustive analysis of the CIBA database derived from the INTERCLE experiment, we used observations made on eight consecutive nights (from 3 to 10 July 2003) to characterize the arrival of a sequence of density currents at the site and to examine the generation of gravity waves for some of the events. During this period, the synoptic situation over the Iberian Peninsula was dominated by an anticyclone with a weak horizontal pressure gradient. Under these conditions, the overviews of each night using data from different levels of the tower show similar evolution for all nights, as we can see in Fig. 2, which presents the time evolution at the CIBA tower for the eight consecutive nights, from 1800 UTC to 0600 UTC. In addition, to see in detail the transition from day to night and the arrival of the density current with an abrupt shift in the mean meteorological variables, Fig. 3 presents their evolution from 1200 UTC on 6 July 2003 to 1200 UTC on 7 July 2003, as a representative example of the period.

An early temperature inversion (Figs. 2, 3a) develops close to the surface along with light north-westerly winds (Figs. 2, 3b,c) just after sunset. However, this situation persists for only a short time, as approximately 1 h later, the wind speed increased abruptly at all levels but most markedly at the highest level of the tower, by nearly  $10 \text{ m s}^{-1}$  at 98.6 m (Figs. 2, 3b) and the wind direction veered significantly towards a north-easterly direction (Figs. 2, 3c). The surface temperature inversion was greatly affected as the sudden change in wind speed and wind direction was accompanied by a rapid fall in temperature, especially at the upper levels (Figs. 2, 3a), which caused a weakening of the thermal inversion after the onset of the density current at the lower levels. These changes suggest the arrival of a cold gravity current from the north-east sector that displaced the air at these levels and forced it upwards, as an updraft current, which is clearly noticeable in the vertical wind-speed measurements, as we will see in Sect. 5.5 below. In addition to these changes, the specific humidity increased at all levels (Figs. 2, 3d), suggesting the arrival of a cold and moist gravity current from the north-east whose origin could have been a diurnal sea breeze originating in the Bay of Biscay in the Cantabrian Sea. This suggestion is supported by the WRF mesoscale simulations presented in the regional scale analysis in Sect. 5.3 below. However, due to the complex topography

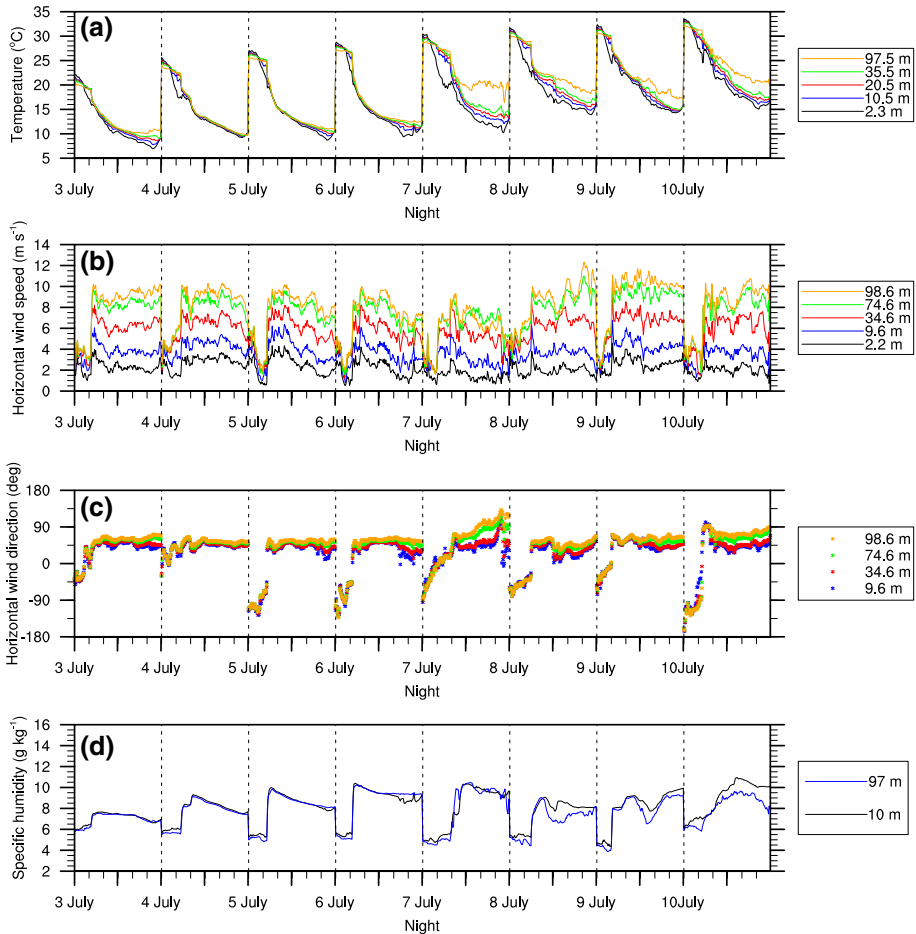


**Fig. 2** Time series for eight consecutive nights (3–10 July 2003) from 1800 UTC to 0600 UTC of: **a** air temperature; **b** wind speed; **c** wind direction, where wind direction values are switched from 000–360 to -180–000–180 with the negative values corresponding to the western quadrant; **d** specific humidity measured at the different levels of CIBA tower (all averaged over a 5-min period)

of the area, this cold and moist flow is reorganized as a set of drainage flows that interact and become an organized north-easterly flow within the Duero basin (Bravo et al. 2008; Cuxart 2008; Martínez et al. 2010). As this coherent structure is also associated with local thermal and shear instabilities (Einaudi and Finnigan 1993; Sun et al. 2002), their effect can also be seen in the TKE and turbulent sensible heat-flux time history, which we calculated every 5 min using the Reynolds decomposition method (Fig. 3e,f) corresponding to 6 July as an example. The values of these quantities increase abruptly with the onset of the density current.

## 5.2 Meteorological Model Evaluation

The WRF meteorological model is used here to compare observations from the CIBA tower (Sect. 5.2.1) and from meteorological stations on the ground distributed over the D2 domain (Sect. 5.2.2) with model simulations at the corresponding nearest grid points.



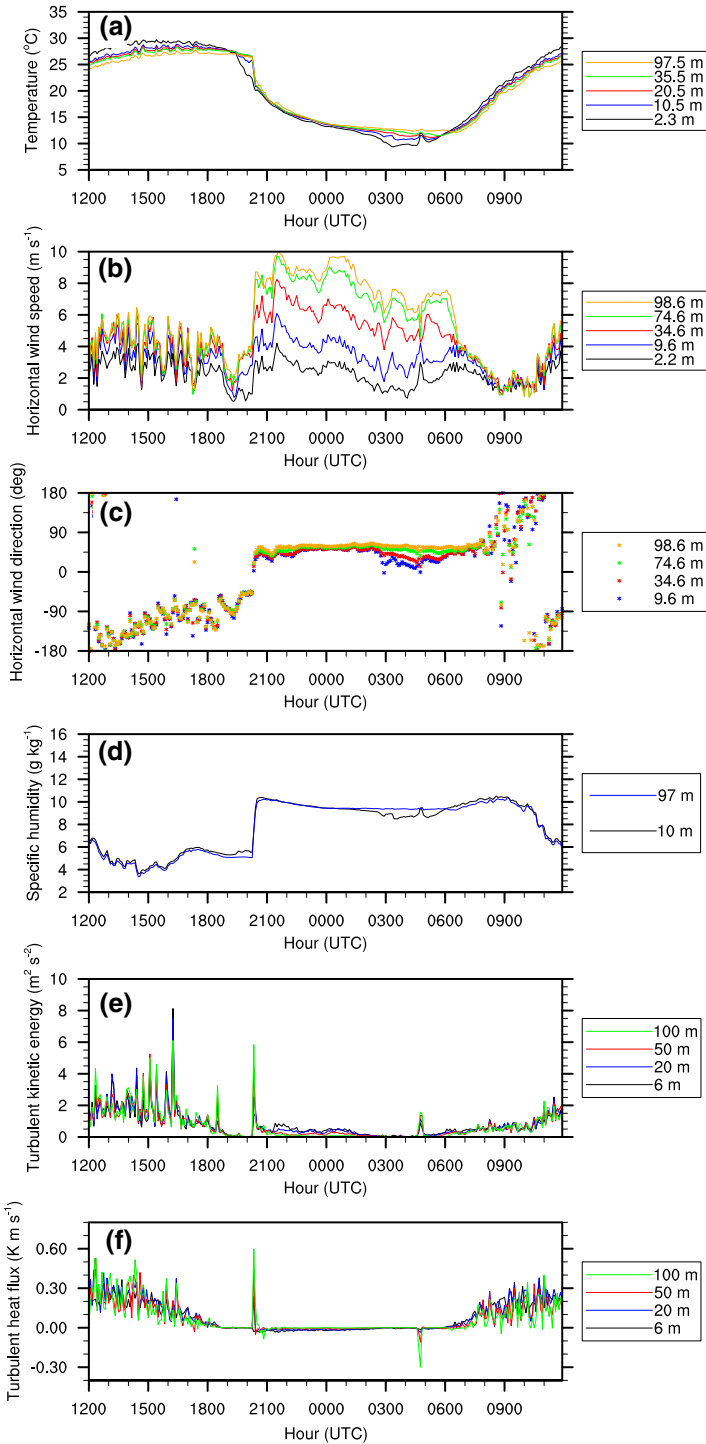


**Fig. 3** Time series from 1200 UTC 5 July 2003 to 1200 UTC 6 July 2003 of: **a** air temperature, **b** wind speed, **c** wind direction, **d** specific humidity, **e** turbulent kinetic energy, and **f** turbulent sensible heat flux measured at the different levels of the CIBA tower (all averaged over a 5-min period)

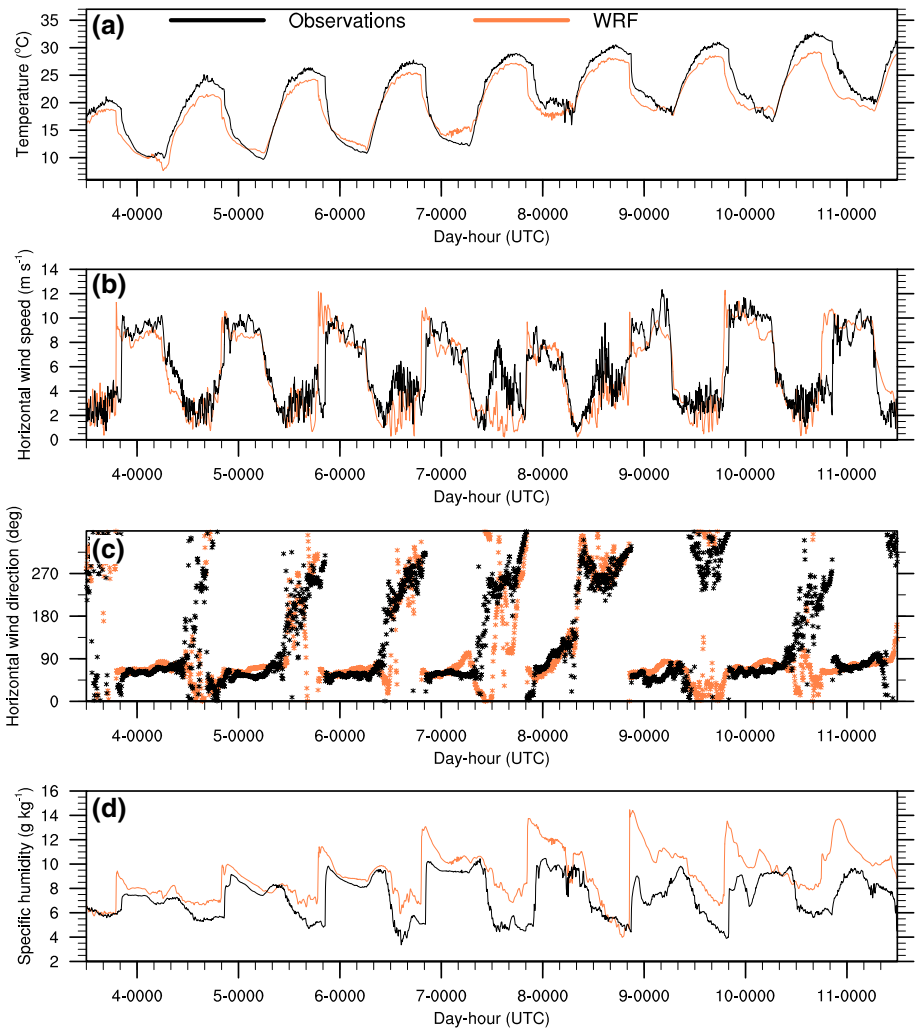


**Fig. 4** Comparison between time series of model simulation (5-min results) and measurements from the highest level of the CIBA tower for all period considered; **a** air temperature, **b** wind speed, **c** wind direction and **d** specific humidity

### 5.2.1 Evaluation at the CIBA Site

The WRF model is evaluated at the CIBA site by: (i) comparing the measured meteorological variables and model results (Figs. 4, 5) in order to analyze the capacity of the model to forecast the density current intrusion and the behaviour of the meteorological variables during its arrival; and (ii) comparing model results and observations from the whole period evaluated, that is from 3 July 2013 at 1200 UTC to 11 July 2013 at 1200 UTC, to analyze the model performance quantitatively.

Daily comparisons of model results with observations for the whole period analyzed indicate that the correspondence of the model to the observations is similar every day.

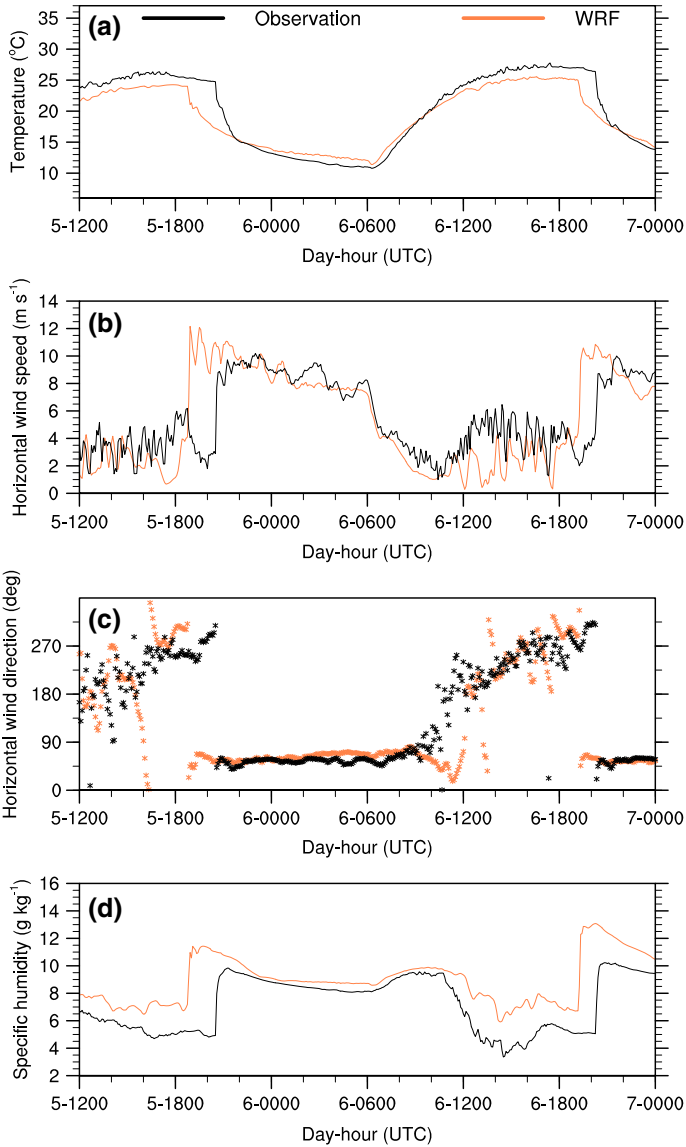


**Fig. 5** Comparison between time series of model simulation (5-min results) and measurements from the highest level of the CIBA tower from 1200 UTC 5 July 2003 to 0000 UTC 7 July 2003; **a** air temperature, **b** wind speed, **c** wind direction and **d** specific humidity

To summarize this information, in Fig. 4 we only present the comparison for the highest level of measurement, the level at which the arrival of the density current is most significant. In addition, to show the model performance in detail, Fig. 5 shows the comparison only for a representative period: from 5 July at 1200 UTC to 7 July 2003 at 0000 UTC. The results show that the model captures the onset of the density current with the corresponding abrupt temperature decrease (Figs. 4, 5a), although its arrival is predicted approximately 90 min early. These results agree with those found in Udina et al. (2013), where the capacity of the

WRF model to simulate gravity waves was compared to using two PBL schemes: the MYJ and Yonsei University (YSU). The model also slightly underestimates maximum temperatures and overestimates minimum temperatures, mainly at the highest measurement level. For wind velocity (Figs. 4, 5b), the model also predicts the arrival early, but is capable of predicting the sharp increase and maintains the high wind speeds at the higher levels of the tower, although the maximum value is overestimated. Moreover, the model captures the shift in wind direction from north–west to north–east at the arrival of the density current, but it also predicts the event too early (Figs. 4, 5c). The model also catches the sharp increase in humidity at 97 m (Figs. 4, 5d), but again it tends to predict it early. Overall, it overestimates the numerical values, mainly in the second part of the period where it overestimates the maximum values.

To evaluate the model performance quantitatively and globally over the simulated period, we have calculated several statistics taking 5-min model results and 5-min averaged Reynolds observations. The mean bias (*MB*) and the root-mean-square error (*RMSE*) were calculated for wind speed; whilst the mean bias and the mean absolute gross error (*MAGE*) were calculated for temperature, wind direction and specific humidity, according to Tesche et al. (2002). The values are summarized in Table 3. For temperature, overall *MAGE* is below the benchmark while *MB* indicates that the model tends to underestimate the temperature, mostly at medium and higher levels where the values are far from the benchmark. The statistics show that the model tends to underestimate wind speed, especially at the higher levels; although the values are slightly below or within the benchmark. Wind direction is not well predicted by the model; *MAGE* is far from the benchmark mainly at the lower levels whilst *MB* values are slightly below the benchmark. These results agree with those of Jiménez et al. (2010) who found that areas with more complex terrain show larger systematic differences in wind direction between model predictions and observations, and these differences depend on wind speed: the greater the wind speed, the smaller the differences in wind direction. Finally, specific humidity is quite well predicted by the model as *MAGE* is overall below the benchmark; *MB* is within the target values and, overall, the model tends to overestimate the specific humidity.

**Table 3** Statistics for air surface temperature, wind speed, wind direction and specific humidity based on CIBA tower values

	Statistic	Benchmark	Levels and values				
Temperature (K)			2.3 m	10.5 m	20.5 m	35.5 m	97.5 m
	<i>MAGE</i>	< 2	1.43	1.48	1.50	1.53	1.87
	<i>MB</i>	< ± 0.5	-0.46	-0.98	-1.12	-1.21	-1.46
Wind speed (m s <sup>-1</sup> )			2.3 m	9.6 m	34.6 m	74.6 m	98.6 m
	<i>RMSE</i>	< 2	1.04	1.37	1.71	1.94	2.03
	<i>MB</i>	< ± 0.5	-0.37	0.01	-0.45	-0.45	-0.34
Wind direction (°)				9.6 m	34.6 m	74.6 m	98.6 m
	<i>MAGE</i>	< 30		42.02	40.58	38.35	38.25
	<i>MB</i>	< ± 10		-13.68	-13.78	-14.70	-15.26
Specific humidity (g kg <sup>-1</sup> )				10 m	97 m		
	<i>MAGE</i>	< 2		1.68	1.84		
	<i>MB</i>	< ± 1		1.62	1.79		

The benchmarks for the statistics are proposed by Tesche et al. (2002) to validate meteorological simulations

**Table 4** Statistics for surface temperature, wind speed and wind direction, based on surface stations values

	Statistic	Benchmark	Values
Temperature (2 m) K	<i>MAGE</i>	< 2	1.90
	<i>MB</i>	< ± 0.5	1.40
Wind speed (10 m) m s <sup>-1</sup>	<i>RMSE</i>	< 2	1.40
	<i>MB</i>	< ± 0.5	0.31
Wind direction (10 m) (°)	<i>MAGE</i>	< 30	64.20
	<i>MB</i>	< ± 0.5	12.80
Specific humidity (2 m) g kg <sup>-1</sup>	<i>MAGE</i>	< 2	1.59
	<i>MB</i>	< ± 1	1.44

The benchmarks for the statistics are proposed by [Tesche et al. \(2002\)](#) to validate meteorological simulations

### 5.2.2 Evaluation at Domain D2

Before analyzing the thermal circulation patterns predicted by the model in the D2 domain, we evaluate the results against observations from 15 ground stations covering this domain (see Fig. 1a). D2 is centred on the CIBA site and covers the area within a radius of 250 km, including the nearest mountain ranges. The statistics were calculated from hourly values for the whole period studied. Temperature at 2 m, both wind speed and direction at 10 m, and specific humidity at 2 m were chosen to calculate the statistics. The values are summarized in Table 4. The statistics indicate that temperature, wind velocity and specific humidity are quite well predicted by the model as the corresponding statistics are overall slightly below or within the benchmarks, but in this case *MB* is positive, indicating that the model overestimates these variables. For wind direction, the statistics are worse, compared to those reported and discussed above.

### 5.3 Vertical Structure of the Density Current

Analysis of the arrival of the sequence of density currents that occurred from 3 to 10 July 2003 shows that their characteristics are very similar; therefore, again, we only consider the most representative nights of the period studied: 5 and 6 July 2003. From the model results, we infer the vertical structure of the density currents (as we had no measurements above 100 m) as well as the mesoscale overview of the wind and temperature fields. This information could be very useful for a detailed study of the flow and the thermal circulation associated with the density current. Time–height diagrams of wind speed and direction as well as of temperature (Fig. 6) show similar behaviour on both days. Before the arrival of the density current, the model predicts westerly winds; after the intrusion, an easterly current about 450 or 350 m thick [corresponding to 5 and 6 July, respectively; Fig. 6a (top and bottom)] is established with a sustained speed of around 10 m s<sup>-1</sup> until nearly midnight. As the night progresses, the thickness of the current decreases and, although the wind direction continues to be from the eastern sector, wind speed begins to decrease especially in the first 100 m. With the arrival of the density current, the vertical thermal structure predicted by the model (Fig. 6b) changes completely; a strong temperature inversion occurs with cold air confined to a layer rising up to a height of 400 or 300 m (corresponding to 5 and 6 July, respectively). After the entrance of the density current, a warm layer is located at a height of approximately 400 or 300 m, respectively (Fig. 6b) since, as the cold current advances, it forces the warm air upwards, just as with the advance of a cold front.

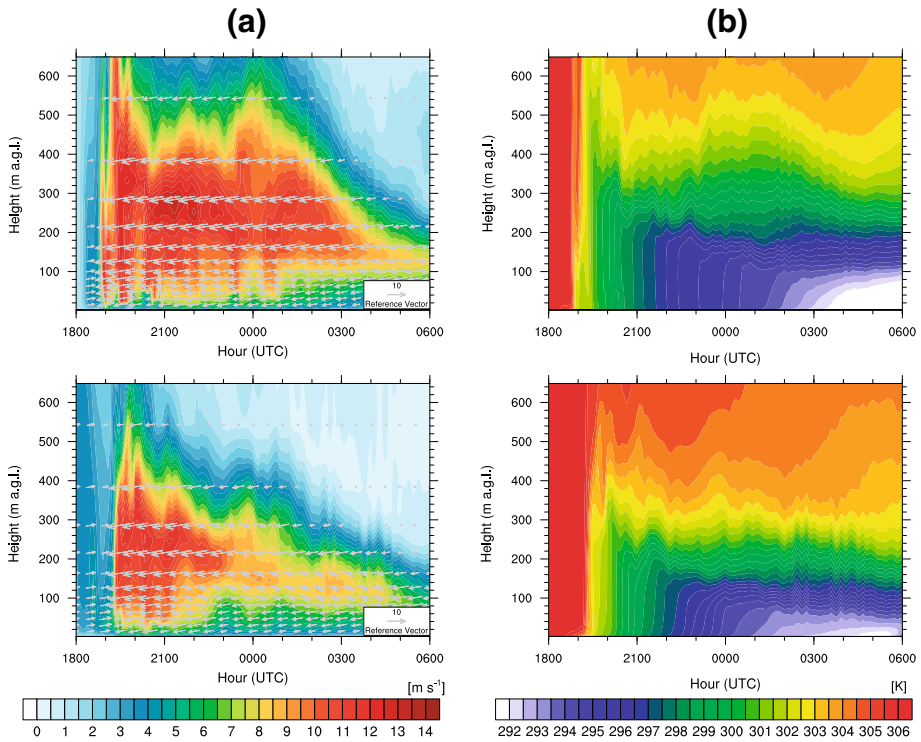


**Fig. 6** Time–height diagram at the CIBA site for the nights of 5 July 2003 (*top*) and 6 July 2003 (*bottom*): **a** simulated wind speed (*shaded*) and horizontal wind direction (*vector*) and **b** simulated potential temperature, using 5-min model results

#### 5.4 Overview of Mesoscale Fields

In order to obtain a detailed picture of the flow and the thermal circulation patterns associated with the sequence of density currents, we analyze the mesoscale overview of the wind, temperature and humidity fields (which cannot be inferred from measurements at one specific site). In this way, in Fig. 7a (left) we see that on 6 July 2003 at 1600 UTC, a cold mass of air from the Cantabrian Sea started moving south-westward far from the CIBA site. Over the following hours, the flow accelerated as it passed over the mountain ranges before arriving at the CIBA site (Fig. 7a, right). This occurred during the transition from day to night, coinciding with the beginning of the establishment of the NBL. From 1600 to 2000 UTC, we also see how the near-surface air temperature falls as the flow moves from north-east to south-west due to the movement of the density current itself. This fall in temperature is also affected, however, by ground radiative cooling that enhances the movement of the current over the mountain slopes located to the north-east of the CIBA site (Fig. 1) via the generation of katabatic flows (Fig. 7b). In Fig. 7c we can likewise see how near-surface specific humidity increases as the moist flow advances from the Cantabrian Sea to the CIBA site. At 100 m a.g.l., the behaviour of the air mass is similar, reaching wind speeds above  $10 \text{ m s}^{-1}$  (not shown). Although these figures correspond to the 6 July 2003, a similar pattern was found during all the periods analyzed.

All our results seem to indicate that the density currents reaching the CIBA site during the eight sequenced days all follow a similar pattern. The flow originated over the Cantabrian



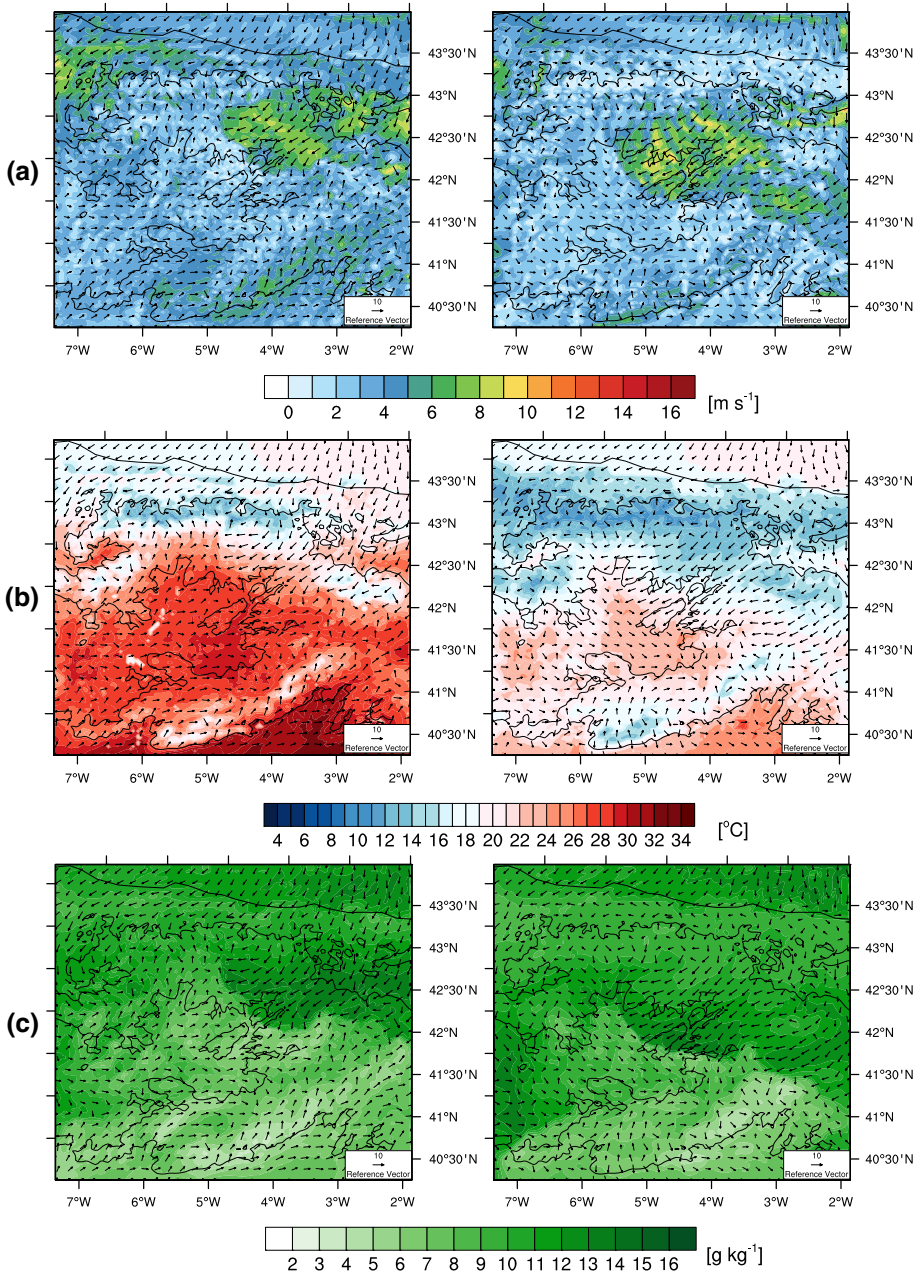


**Fig. 7** Second domain model results for 5 July 2003 at 1600 UTC (left) and 2000 UTC (right) of: **a** 10-m wind speed (shaded) and 10-m horizontal wind vectors, **b** 2-m air temperature (shaded) and 10-m horizontal wind vectors, **c** 2-m specific humidity (shaded) and 10-m horizontal wind vectors. Black contour lines correspond to 800-m terrain height

Sea and was strongly perturbed by topographical features as it crossed the mountain range located to the north-east of the D2 domain. The flows over sloping terrain were accelerated due to pressure and temperature gradients. So, both the entrance of the sea breeze and the

katabatic flow constituted the origin of the cold density current that moved rapidly as the surface cooled. The topographical effects become even more decisive and the air mass from the north–east accelerated even more so in the model. This would also explain why the model anticipated the event, since it overestimates the cooling rate (as shown by the ground station statistics). So, this cold and moist gravity current moved rapidly with enhanced turbulence. Sun et al. (2002) and Udina et al. (2013) similarly analyzed a wind surge and a temperature fall that revealed the passage of a density current associated with intermittent turbulence.

### 5.5 Observed Gravity Waves

To analyze the possibility of the density currents inducing gravity waves, we carried out a detailed study of the temperature and velocity components measured by the sonic anemometers on the CIBA tower. Our results show the following common characteristics for all the days analyzed: (i) the arrival of the density current is characterized by a sudden increase in vertical velocity, clearly visible in the highest measurements, and a sudden decrease in temperature, clearly visible at all levels; (ii) the onset of the density current is followed by a period of intense turbulent activity.

After the phase of intense turbulence, however, traces of internal gravity waves were only detected on two nights: 5 and 6 July 2003. On those nights, the temperature and vertical velocity measurements (Fig. 8a, b corresponding to 5 July 2003) show periods of lower amplitude oscillations (A and B) clearly seen at the highest level of the tower for temperature and less evident in vertical velocity. The most likely reason for these oscillations is a gravity wave induced by the arrival of the density current that forces the air to rise and causes the air parcels to cool. However, a parcel of air displaced upwards in the stable boundary layer will encounter a restoring force due, precisely, to the stability; the parcel will then accelerate downwards, leading to the warming of the air parcel. This process can create the oscillatory behaviour observed before 2100 UTC (A) and after 2115 UTC (B) with time periods of around 6.5 and 8 min, respectively. In addition, the temperature oscillations occur around 1.6 (A) and 2 (B) min ahead of the vertical velocity oscillations (Fig. 8c); values that are near a quarter of the estimated wave periods (about 6.5 and 8 min, respectively). These results are consistent with linear wave theory, which predicts that temperature and vertical velocity oscillations should be  $\pm 90^\circ$  out of phase. The Brunt–Väisälä frequency as estimated from vertical profiles of potential temperature was around  $0.022 \text{ s}^{-1}$ , which is higher than the frequency of the observed wave (about  $0.0025$  and  $0.0020 \text{ s}^{-1}$ ), implying that the observed propagating wave was an internal gravity wave (Gill 1982).

The arrival of the density currents was also analyzed employing the wavelet method described in Sect. 3, using a 6-base-frequency Morlet function with integration up to a 30-min period. The numerical results calculated from the data obtained from sonic anemometers located at different levels on the CIBA tower between 1900 and 2200 UTC during the period analyzed are presented as a detailed time–period representation of kinetic energy density per unit period (in  $\text{m}^2 \text{ s}^{-3}$ ) and heat-flux density per unit period ( $\text{K m s}^{-2}$ ) in Figs. 9 and 10. As elsewhere, we only present results corresponding to some events: those corresponding to 5, 6 and 8 July 2003. Figure 9a, corresponding to 5 July 2003, shows several peaks for low periods, which can be attributed to bursts of turbulence, and an elongated coherent structure detected at all levels, the energy of which was spread out over a wide spectral range. This elongated structure, denoting a sudden change in the prevailing conditions (Terradellas et al. 2005), coincides with the gravity current that occurred at 2030 UTC, which also appears in Fig. 9b at 2155 UTC and Fig. 9c at 2100 UTC (corresponding to 6 and 8 July 2003, respectively). However, in Fig. 9a, as well as this structure, we see high values of kinetic energy



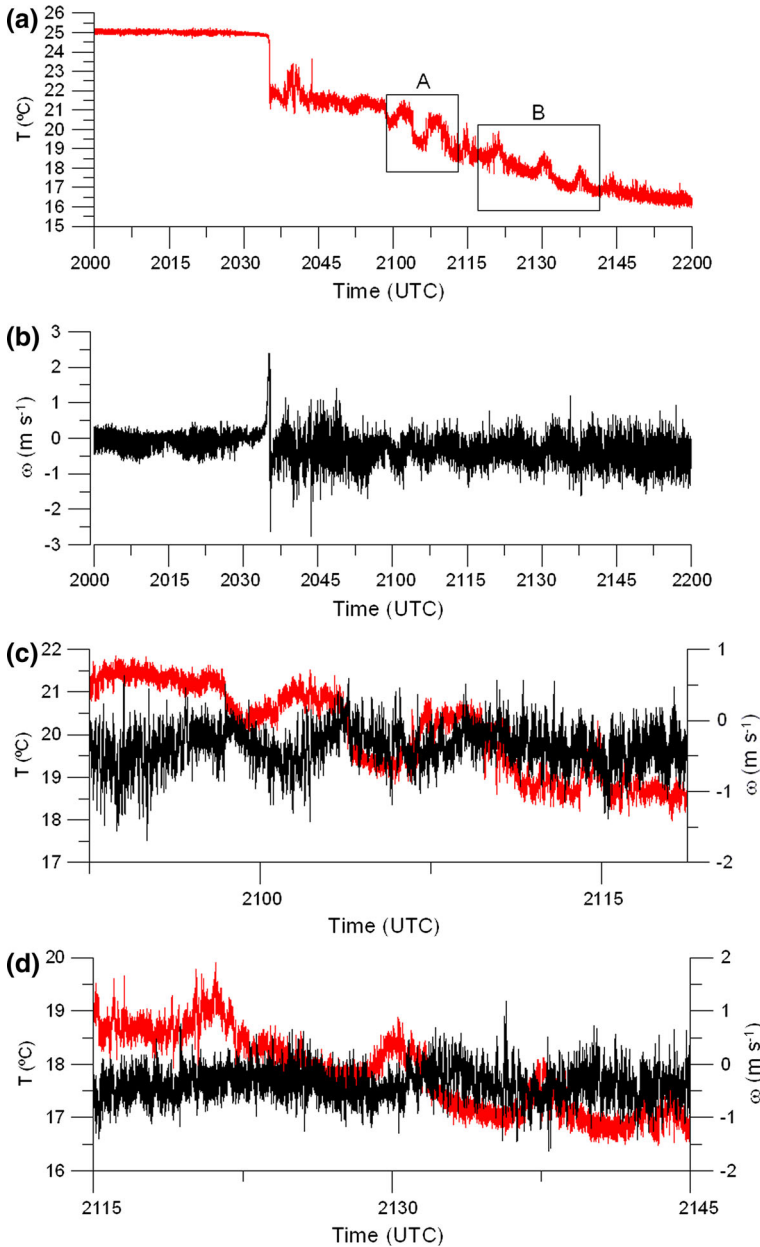


**Fig. 8** Time series recorded at the highest level of the tower during 5 July 2003 of: **a** air temperature, **b** vertical velocity, **c** and **d** detailed time evolution of air temperature and vertical velocity. Temperature oscillations at different time intervals, *A* and *B*, are labelled by a *rectangle*

density that are constrained to a relatively narrow range of periods centred on approximately 6.5 and 8 min, respectively, which correspond to the periods of the internal gravity waves found from the measurements. In Fig. 9b we observe similar behaviour; besides the elongated structure, we can also see high values of kinetic energy density constrained to a relatively

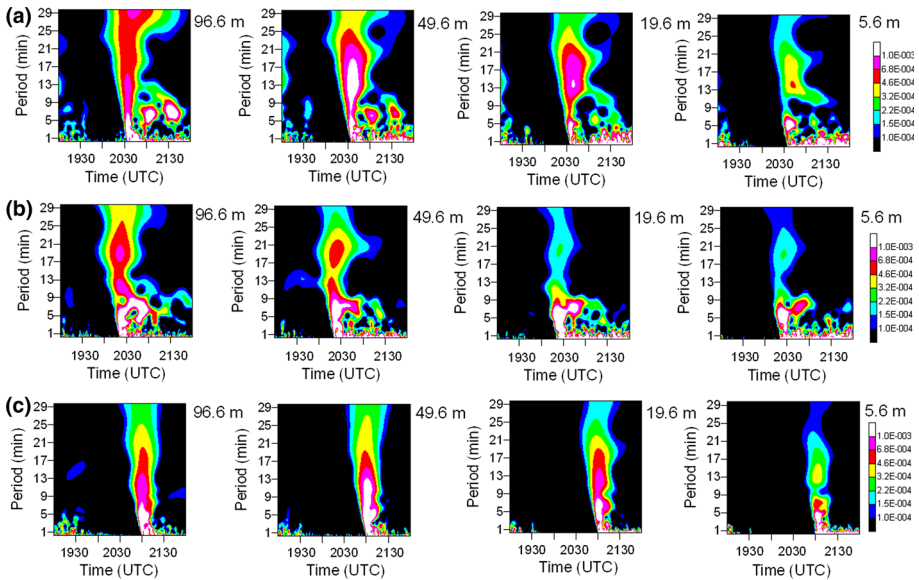


**Fig. 9** Time–period representation of kinetic energy density per unit period (in  $\text{m}^2 \text{s}^{-3}$ ) at different CIBA tower levels during the night 5 July 2003 (a), 6 July 2003 (b) and 8 July 2003 (c)

narrow range of periods, centred at about 6.5 min, which matches with the internal gravity waves found on 6 July 2003 from the measurements. Finally, in Fig. 9c we did not detect any structure other than the gravity current from the tower measurements.

The capacity of wavelet-based techniques to analyze the separate contributions of different spectral ranges to the total energy or fluxes enabled us to examine the physical reasons for the alternation of the sign of the vertical heat-flux density per unit period depicted in Fig. 10a,b (corresponding to 5 and 6 July 2003) mainly at the highest level. A plausible explanation of this behaviour in the context of a density current is based on the following conceptual model: a downward-moving cold air parcel warms adiabatically, reaching and then exceeding its equilibrium level, becoming a downward warm current. Similarly, an upward-moving warm air parcel cools adiabatically, exceeds its equilibrium level and becomes an upward cold current. This double circulation is in close agreement with the continuity condition (Terradellas et al. 2005).

## 6 Conclusions

Observations gathered from a 100-m meteorological tower located in Spain have allowed us to detect and characterize a sequence of eight density currents observed in the late evening, between 2000 and 2200 UTC, on eight consecutive days in July 2003. Their analysis has showed that all the density currents have the following common features: (1) a sudden decrease in air temperature; (2) an abrupt increase in wind speed; (3) a rapid shift in wind direction; (4) a sudden increase in water vapour mixing ratio; and (5) a rapid increase in turbulence intensity manifest as an increase of vertical velocity, TKE and vertical sensible heat flux.

The results of our observations were complemented with model simulations, since a single point of measurement is insufficient to analyze the origin of the cold density currents

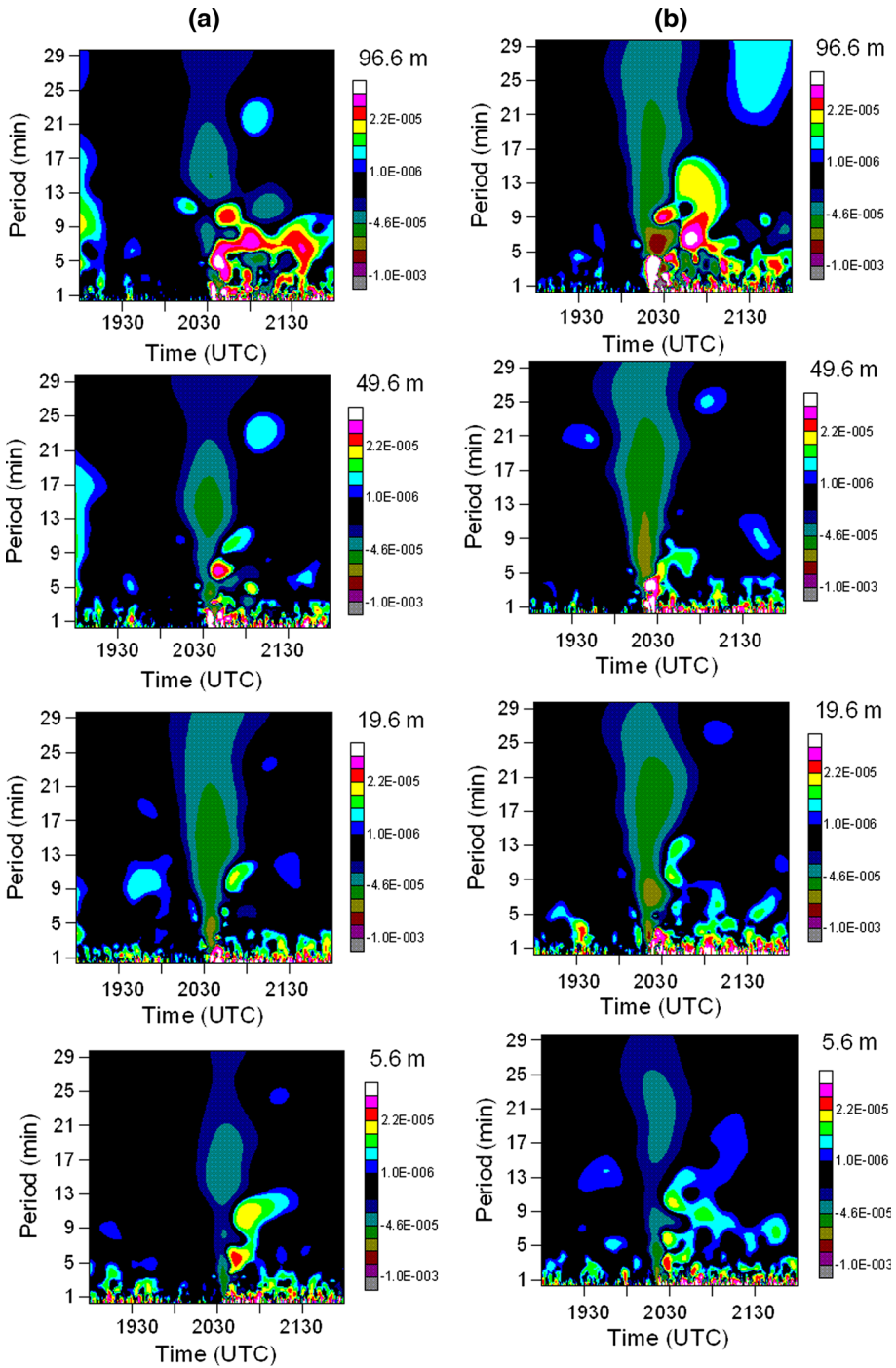


**Fig. 10** Time–period representation of heat flux density per unit period ( $\text{K m s}^{-2}$ ) at different CIBA tower levels during the night 5 July 2003 (a) and 6 July 2003 (b)

observed at the CIBA tower and the thermal flows driven by the complex topography of the area studied. We have shown that the WRF model is capable of simulating the gravity currents and their arrival, although it presents some discrepancies with measurements, mainly the time gap, as the model predicts an early onset of the density current. The observations and especially the model simulations support the hypothesis that the density currents originate over the Cantabrian Sea and are strongly perturbed by topographical features when crossing the mountain range located in the north–east part of the area studied. Therefore, the entrance of the sea breeze and the katabatic flow were the origin of the cold and moist density currents advancing southward from the Cantabrian Sea onto the northern Castile plateau.

Wavelet analysis applied to the measurements illustrated and proved that this method has the capacity to distinguish the arrival of the density current, the different scales involved in the event due to the different timing, the heights of the thermal instabilities and downdrafts associated with this atmospheric disturbance, as well as the small-scale turbulence induced by these processes. It has also been demonstrated that the wavelet method is a good technique to detect the presence of gravity waves in the atmospheric boundary layer which, as in this case, are induced by the arrival of a density current.

**Acknowledgments** This study was supported by the Spanish government through the project CGL 2012-37416-C04-04. The authors would like to thank the University of Valladolid for their contribution in obtaining the CIBA tower dataset used in this study. ECMWF ERA-Interim data used in this study have been obtained from the ECMWF Data Server.

## References

- Acevedo OC, Fitzjarrald DR (2003) In the core of the night-effects of intermittent mixing on a horizontally heterogeneous surface. *Boundary-Layer Meteorol* 106:1–33
- Adachi A, Clark WL, Hartten LM, Gage KS, Kobayashi T (2004) An observational study of a shallow gravity current triggered by katabatic flow. *Ann Geophys* 22:3937–3950
- Arnold D, Morton D, Schicker I, Seibert P, Rotach M, Horvath K, Dudhia J, Satomura T, Müller M, Zängl G, Takemi T, Serafin S, Schmidli J, Schneider S (2012) High resolution modelling in complex terrain. Report on the HiRCoT 2012 Workshop, Vienna, 21–23 Feb 2012
- Balsley BB, Frehlich RG, Jensen ML (2002) Preliminary CASES-99 measurements of steep vertical gradients in temperature and turbulence structure using a tethered lifting system (TLS). In: American Meteorological Society (ed) 15th Symposium on boundary layers and turbulence, Wageningen, 15–19 July 2002, pp 461–464
- Banta RM (2008) Stable-boundary-layer regimes from the perspective of the low-level jet. *Acta Geophys* 56:58–87
- Barry RG (1992) Mountain, weather and climate. Psychology Press, Hove 402 pp
- Beljaars ACM (1994) The parameterization of surface fluxes in large-scale models under free convection. *Q J R Meteorol Soc* 121:255–270
- Blumen W, Banta R, Burns SP, Fritts DC, Newsom R, Poulos GS, Sun J (2001) Turbulence statistics of a Kelvin–Helmholtz billow event observed in the night-time boundary layer during the Cooperative Atmosphere–Surface Exchange Study field program. *Dyn Atmos Ocean* 34:189–204
- Bravo M, Mira T, Soler MR, Cuxart J (2008) Intercomparison and evaluation of MM5 and Meso-NH mesoscale models in the stable boundary layer. *Boundary-Layer Meteorol* 128:77–101
- Chemel C, Staquet C, Largeron Y (2009) Generation of internal gravity waves by a katabatic wind in an idealized alpine valley. *Meteorol Atmos Phys* 103:187–194. doi:10.1007/s00703-009-0349-4
- Chen F, Dudhia J (2001) Coupling an advanced land surface-hydrology model with the Penn State-NCAR MM5 modeling system. Part I: model implementation and sensitivity. *Mon Weather Rev* 129:569–585
- Conangla L, Cuxart J, Soler MR (2008) Characterisation of the nocturnal boundary layer at a site in northern Spain. *Boundary-Layer Meteorol* 128:255–276
- Coulter RL, Doran JC (2002) Spatial and temporal occurrences of intermittent turbulence during CASES-99. *Boundary-Layer Meteorol* 105:329–349
- Cuxart J (2008) Nocturnal basin low-level jets: an integrated study. *Acta Geophys* 56:100–113

- Cuxart J, Jiménez MA (2007) Mixing processes in a nocturnal low-level jet: an LES study. *J Atmos Sci* 64:1666–1679
- Cuxart J, Morales G, Terradellas E, Yagüe C (2002) Study of coherent structures and estimation of the pressure transport terms for the nocturnal stable boundary layer. *Boundary-Layer Meteorol* 105:305–328
- Cuxart J, Yagüe C, Morales G, Terradellas E, Orbe J, Calvo J, Fernandez A, Soler MR, Infante C, Buenestado P, Espinald A, Joergensen H, Rees J, Vila J, Redondo J, Cantalapiedra I, Conangla L (2000) Stable atmospheric boundary-layer experiment in Spain (SABLES 98): a report. *Boundary-Layer Meteorol* 96:337–370
- Daubechies I (1992) Ten lectures on wavelets. CBMS-NSF Lecture Notes nr. 61. SIAM, Philadelphia 354 pp
- Dudhia J (1989) Numerical study of convection observed during the winter monsoon experiment using a mesoscale two-dimensional model. *J Atmos Sci* 46:3077–3107
- Einaudi F, Finnigan JJ (1993) Wave-turbulence dynamics in the stably stratified boundary layer. *J Atmos Sci* 50:1841–1864
- Fritts DC, Nappo C, Riggan DM, Balsley BB, Eichinger WE, Newsom RK (2003) Analysis of ducted motions in the stable nocturnal boundary layer during CASES-99. *J Atmos Sci* 60:2450–2472
- Gill AE (1982) Atmosphere–ocean dynamics. Academic Press, New York 662 pp
- Hu X, Nielsen-Gammon JW, Zhang F (2010) Evaluation of three planetary boundary layer schemes in the WRF model. *J Appl Meteorol Climatol* 49:1831–1844
- Janjić ZI (1996) The surface layer in the NCEP Eta Model. Eleventh conference on numerical weather prediction, Norfolk, 19–23 Aug
- Janjić ZI (1990) The step-mountain coordinate: physical package. *Mon Weather Rev* 118:1429–1443
- Janjić ZI (1994) The step-mountain eta coordinate model: further development of the convection, viscous sublayer, and turbulence closure schemes. *Mon Weather Rev* 122:927–945
- Janjić ZI (2002) Nonsingular implementation of the Mellor–Yamada level 2.5 scheme in the NCEP Meso model. NCEP Off Note 437:61
- Jiménez PA, González-Rouco JF, García-Bustamante E, Navarro J, Montavez JP, Dudhia J, Roldan A (2010) Surface wind regionalization over complex terrain: evaluation and analysis of a high-resolution WRF simulation. *J Appl Meteorol Climatol* 49:268–287
- Maguire AJ, Rees JM, Derbyshire SH (2006) Stable atmospheric boundary layer over a uniform slope: some theoretical concepts. *Boundary-Layer Meteorol* 120:219–227
- Mahrt L (1999) Stratified atmospheric boundary layers. *Boundary-Layer Meteorol* 90:375–396
- Mahrt L (1989) Intermittent of atmospheric turbulence. *J Atmos Sci* 46:79–95
- Mahrt L, Vickers D, Nakamura R, Soler MR, Sun J, Burns SP, Lenschow DH (2001) Shallow drainage flows. *Boundary-Layer Meteorol* 101:243–260
- Mallat S (1999) A wavelet tour of signal processing. Academic Press, San Diego 620 pp
- Martínez D, Cuxart J (2009) Assessment of the hydraulic slope flow approach using a mesoscale model. *Acta Geophys* 57:882–903
- Martínez D, Jiménez MA, Cuxart J, Mahrt L (2010) Heterogeneous nocturnal cooling in a large basin under very stable conditions. *Boundary-Layer Meteorol* 137:97–113
- Mayor SD (2011) Observations of seven atmospheric density current fronts in Dixon, California. *Mon Weather Rev* 139:1338–1351
- Meillier YP, Frehlich RG, Jones RM, Balsley BB (2008) Modulation of small-scale turbulence by ducted gravity waves in the nocturnal boundary layer. *J Atmos Sci* 65:1414–1427
- Mellor GL, Yamada T (1982) Development of a turbulence closure model for geophysical fluid problems. *Rev Geophys Space Phys* 20:851–875
- Meyers SD, Kelly BG, O'Brien JJ (1993) An introduction to wavelet analysis in oceanography and meteorology: with application to the dispersion of Yanai waves. *Mon Weather Rev* 121:2858–2866
- Mlawer EJ, Taubman SJ, Brown PD, Iacono MJ, Clough SA (1997) Radiative transfer for inhomogeneous atmospheres: RRTM, a validated correlated-k model for the longwave. *J Geophys Res* 102:16616–16663
- Monin AS, Obukhov AM (1954) Basic laws of turbulent mixing in the surface layer of the atmosphere. *Contrib Geophys Inst Acad Sci USSR* 151:163–187
- Nappo C (1991) Sporadic breakdowns of stability in the PBL over simple and complex terrain. *Boundary-Layer Meteorol* 54:69–87
- Newsom RK, Banta RM (2003) Shear-flow instability in the stable nocturnal boundary layer as observed by Doppler lidar during CASES-99. *J Atmos Sci* 60:16–33
- Poulos GS, Blumen W, Fritts DC, Lundquist JK, Sun J, Burns SP, Balsley BB, Jensen M (2002) CASES-99: a comprehensive investigation of the stable nocturnal boundary layer. *Bull Am Meteorol Soc* 83:555–581
- Prabha TV, Leclerc MY, Karipot A, Hollinger DY (2007) Low-frequency effects on eddy covariance fluxes under the influence of a low-level jet. *J Appl Meteorol Climatol* 46:338–352

- Seaman NL, Gaudet BJ, Stauffer DR, Mahrt L, Richardson SJ, Zielonka JR, Wyngaard JC (2012) Numerical prediction of submesoscale flow in the nocturnal stable boundary layer over complex terrain. *Mon Weather Rev* 140:956–977
- Skamarock WC, Klemp JB, Dudhia J, Gill DO, Barker DM, Wang W, Powers JG (2008) A description of the advanced research WRF Version 3. NCAR Technical Notes-475+ STR
- Shin HH, Hong S (2011) Intercomparison of planetary boundary-layer parametrizations in the WRF model for a single day from CASES-99. *Boundary-Layer Meteorol* 139:261–281
- Soler MR, Infante C, Buenestado P, Mahrt L (2002) Observations of nocturnal drainage flow in a shallow gully. *Boundary-Layer Meteorol* 105:253–273
- Sun J (2011) Vertical variations of mixing lengths under neutral and stable conditions during CASES-99. *J Appl Meteorol* 50:2030–2041
- Sun J, Burns SP, Lenschow DH, Banta RM, Newsom RK, Coulter R, Frasier S, Ince T, Nappo C, Blumen W, Lee X, Hu XZ (2002) Intermittent turbulence associated with a density current passage in the stable boundary layer. *Boundary-Layer Meteorol* 105:199–219
- Sun J, Lenschow DH, Burns SP, Banta RM, Newsom RK, Coulter R, Frasier S, Ince T, Nappo C, Balsley BB, Jensen M, Mahrt L, Miller D, Skelly B (2004) Atmospheric disturbances that generate intermittent turbulence in nocturnal boundary layers. *Boundary-Layer Meteorol* 110:255–279
- Terradellas E, Morales G, Cuxart J, Yagüe C (2001) Wavelet methods: application to the study of the stable atmospheric boundary layer under non-stationary conditions. *Dyn Atmos Ocean* 34:225–244
- Terradellas E, Soler MR, Ferreres E, Bravo M (2005) Analysis of oscillations in the stable atmospheric boundary layer using wavelet methods. *Boundary-Layer Meteorol* 114:489–518
- Tesche TW, McNally DE, Tremback C (2002) Operational evaluation of the MM5 meteorological model over the continental United States: protocol for annual and episodic evaluation. Wright, KY, and ATMET Inc., Boulder. Prepared for US EPA by Alpine Geophysics, LLC, Ft. Wright
- Thompson G, Rasmussen RM, Manning K (2004) Explicit forecasts of winter precipitation using an improved bulk microphysics scheme. Part I: description and sensitivity analysis. *Mon Weather Rev* 132:519–542
- Torrence C, Compo GP (1998) A practical guide to wavelet analysis. *Bull Am Meteorol Soc* 79:61–78
- Udina M, Soler MR, Viana S, Yagüe C (2013) Model simulation of gravity waves triggered by a density current. *Q J R Meteorol Soc* 139:701–714. doi:10.1002/qj.2004
- Viana S, Terradellas E, Yagüe C (2010) Analysis of gravity waves generated at the top of a drainage flow. *J Atmos Sci* 67:3949–3966
- Viana S, Yagüe C, Maqueda G (2009) Propagation and effects of a mesoscale gravity wave over a weakly-stratified nocturnal boundary layer during the SABLES2006 field campaign. *Boundary-Layer Meteorol* 133:165–188
- Viana S, Yagüe C, Maqueda G, Morales G (2007) Study of the surface pressure fluctuations generated by waves and turbulence in the nocturnal boundary layer during SABLES2006 field campaign. *Física la Tierra* 19:55–71
- Yagüe C, Viana S, Maqueda G, Lazcanos MF, Morales G, Rees J (2007) A study on the nocturnal atmospheric boundary layer: SABLES2006. *Física la Tierra* 19:37–53
- Zilitinkevich SS (1995) Non-local turbulent transport: pollution dispersion aspects of coherent structure of convective flows. In: Power H, Moussiopoulos N, Brebbia CA (eds) *Air pollution III—vol I: Air pollution theory and simulation*. Computational Mechanics Publications, Southampton, pp 53–60